



# AMERICAN METEOROLOGICAL SOCIETY

*Journal of Applied Meteorology and Climatology*

## **EARLY ONLINE RELEASE**

This is a preliminary PDF of the author-produced manuscript that has been peer-reviewed and accepted for publication. Since it is being posted so soon after acceptance, it has not yet been copyedited, formatted, or processed by AMS Publications. This preliminary version of the manuscript may be downloaded, distributed, and cited, but please be aware that there will be visual differences and possibly some content differences between this version and the final published version.

The DOI for this manuscript is doi: 10.1175/JAMC-D-14-0053.1

The final published version of this manuscript will replace the preliminary version at the above DOI once it is available.

If you would like to cite this EOR in a separate work, please use the following full citation:

Williams, A., R. Seager, M. Berkelhammer, A. Macalady, M. Crimmins, T. Swetnam, A. Trugman, N. Buening, N. Hryniw, N. McDowell, D. Noone, C. Mora, and T. Rahn, 2014: Causes and Implications of Extreme Atmospheric Moisture Demand during the Record-Breaking 2011 Wildfire Season in the Southwest United States. *J. Appl. Meteor. Climatol.* doi:10.1175/JAMC-D-14-0053.1, in press.



## Causes and implications of extreme atmospheric moisture demand during the record-breaking 2011 wildfire season in the southwest United States

A. Park Williams, Richard Seager, Max Berkelhammer, Alison K. Macalady, Michael A. Crimmins, Thomas W. Swetnam, Anna T. Trugman, Nikolaus Buenning, Natalia Hryniw, Nate G. McDowell, David Noone, Claudia I. Mora, Thom Rahn

\*A. Park Williams, corresponding author  
Biology and Paleo Environment  
Lamont-Doherty Earth Observatory of  
Columbia University  
61 Route 9W  
Palisades, NY 10964, USA  
williams@ldeo.columbia.edu  
845-365-8193

Richard Seager  
Lamont Doherty Earth Observatory of  
Columbia University

Max Berkelhammer  
Dept. of Atmospheric & Oceanic Sciences  
Cooperative Institute for Research in  
Environmental Sciences  
University of Colorado

Alison K. Macalady  
School of Geography and Development  
Laboratory of Tree-Ring Research  
University of Arizona

Michael A. Crimmins  
College of Agriculture and Life Sciences  
University of Arizona

Thomas W. Swetnam  
Laboratory of Tree-ring Research  
University of Arizona

Anna T. Trugman  
Dept. of Atmospheric and Oceanic Sciences  
Princeton University

Nikolaus Buenning  
Department of Earth Sciences  
University of Southern California

Natalia Hryniw  
Department of Atmospheric Sciences  
University of Washington

Nate G. McDowell  
Earth & Environmental Sciences Division  
Los Alamos National Laboratory

David Noone  
Dept. of Atmospheric & Oceanic Sciences  
Cooperative Institute for Research in  
Environmental Sciences  
University of Colorado

Claudia I. Mora  
Earth & Environmental Sciences Division  
Los Alamos National Laboratory

Thom Rahn  
Earth & Environmental Sciences Division  
Los Alamos National Laboratory

1 **Abstract**

2 In 2011, exceptionally low atmospheric moisture content combined with moderately high  
3 temperatures to produce record-high vapor-pressure deficit (VPD) in the southwestern United  
4 States (SW). These conditions combined with record-low cold-season precipitation to cause  
5 widespread drought and extreme wildfires. Although interannual VPD variability is generally  
6 dominated by temperature, high VPD in 2011 was also driven by lack of atmospheric moisture.  
7 May–July 2011 dew point in the SW was 5.1 standard deviations below the long-term mean.  
8 Lack of atmospheric moisture was promoted by already very dry soils and amplified by a strong  
9 ocean-to-continent sea-level pressure gradient and upper-level convergence that drove dry  
10 northerly winds and subsidence upwind of and over the SW. Subsidence drove divergence of  
11 rapid and dry surface winds over the SW, suppressing southerly moisture imports and removing  
12 moisture from already dry soils. By the 2050s, model projections developed for the fifth phase of  
13 the Coupled Model Intercomparison Project (CMIP5) suggest that warming trends will cause  
14 mean warm-season VPD to be comparable to the record-high VPD observed in 2011. CMIP5  
15 projections also suggest increased interannual variability of VPD, independent of trends in  
16 background mean levels, due to increased variability of dew point, temperature, vapor pressure,  
17 and saturation vapor pressure. Increased variability in VPD translates to increased probability of  
18 2011-type VPD anomalies, which would be superimposed on ever-greater background VPD  
19 levels. While temperature will continue to be the primary driver of interannual VPD variability,  
20 2011 served as an important reminder that atmospheric moisture content can also drive impactful  
21 VPD anomalies.

22

23

24 **1. Introduction**

25 The southwest United States (SW) experienced extreme drought in 2011, related at least in part  
26 to a La Niña event in the tropical Pacific Ocean (Rupp et al. 2012; Hoerling et al. 2013; Seager et  
27 al. 2014). The 2011 SW drought event was accompanied by record-breaking total burned area  
28 (Williams et al. in press) and record-size “megafires” in the forests of eastern Arizona and  
29 northern New Mexico. Extreme drought and wildfire conditions prompted widespread concern as  
30 to whether the anomalous 2011 conditions foreshadowed continued intensification of regional  
31 drought-driven wildfires in the SW due to greenhouse warming (e.g., Miller 2012; Nijhuis 2012).

32

33 Temperature has been shown to influence wildfire behavior in the SW by positively influencing  
34 drought (e.g., Westerling et al. 2006; Littell et al. 2009; Abatzoglou and Kolden 2013). The  
35 effect of temperature on drought operates via an exponential forcing on atmospheric moisture  
36 demand, or vapor-pressure deficit (VPD) (Anderson 1936; Williams et al. 2013; Williams et al.  
37 in press). VPD is defined as atmospheric saturation vapor pressure (the water-vapor holding  
38 capacity, which is purely a function of temperature) minus actual vapor pressure. Therefore, the  
39 influence of temperature on drought conditions can be mitigated or amplified by variations in  
40 atmospheric moisture content. Importantly, temperature exponentially influences VPD via its  
41 Clausius-Clapeyron effect on saturation vapor pressure.

42

43 In 2011, very large burned area co-occurred with high moisture deficit (driven by high VPD and  
44 low precipitation), consistent with the well-known positive correlation between drought and  
45 wildfire in the region (e.g., Swetnam and Betancourt 1990, 1998; Westerling et al. 2003;  
46 Westerling and Swetnam 2003; Westerling et al. 2006; Littell et al. 2009; Abatzoglou and

47 Kolden 2013; Williams et al. 2013; Williams et al. in press). While the causes of low cold-season  
48 precipitation in 2010–2011 (which only reached extreme anomalies in Texas, east New Mexico,  
49 and Mexico) have been diagnosed (Hoerling et al. 2013; Seager et al. 2014), causes of extreme  
50 warm-season VPD have not. Here we diagnose the large-scale climate processes that resulted in  
51 exceptionally high VPD in 2011. We then evaluate modeled projections to better understand  
52 how, if at all, the processes causing extreme 2011 VPD anomalies are projected to change in the  
53 future. We also evaluate projected changes in the interannual variability of VPD and its sub-  
54 components to understand projected changes in the frequencies of extreme temperature,  
55 humidity, and VPD excursions that are superimposed upon projected background trends.

56

## 57 **2. Data and methods**

58 We define the SW as the areas of Arizona, New Mexico, Texas, Oklahoma, Colorado, and Utah  
59 that lie south of 38°N, north of 28.5°N, and west of 100°W (as in Williams et al. in press). We  
60 used the ~4 km gridded monthly (January 1895 – June 2014) PRISM dataset developed at  
61 Oregon State University (accessed July 2014) to evaluate precipitation, maximum daily  
62 temperature ( $T_{\max}$ ), minimum daily temperature ( $T_{\min}$ ), dew point, and VPD anomalies (VPD  
63 calculated as in Williams et al. 2013). Precipitation and temperature data come from the latest  
64 version of the PRISM dataset ([www.prism.oregonstate.edu](http://www.prism.oregonstate.edu)) but dew point data come from the  
65 previous version (<http://oldprism.nacse.org>) because dew-point data are not yet included in the  
66 new dataset. We calculate VPD using temperature from the old dataset through 2013 to be  
67 consistent with the dew point data. We calculate 2014 VPD using new-dataset temperature  
68 because the old-dataset temperature record ends in 2013. Although PRISM may not be ideal for  
69 evaluating long-term trends or temporal anomalies at some specific locations or regions (e.g.,

70 Hamlet and Lettenmaier 2005), Williams et al. (in press) demonstrate that PRISM climate  
71 records for the SW are comparable to those calculated using a wide variety of data products. An  
72 exception is for records of atmospheric moisture (dew point) prior to 1961, when station-based  
73 humidity measurements were rare. We therefore report dew point and VPD anomalies relative to  
74 both the post-1895 and post-1961 periods.

75  
76 Additionally, we accessed surface wind-speed (hourly) and soil moisture (monthly) data gridded  
77 at  $0.125^\circ$  resolution from the North American Land Data Assimilation System project phase 2  
78 (NLDAS-2, Mitchell et al. 2004) for 1979–2014. NLDAS-2 near-surface (10 m) wind data are  
79 based upon the National Center for Environmental Protection’s (NCEP’s) 3-hourly, 32-km North  
80 America Regional Reanalysis (NARR), produced using an assimilation of surface measurements,  
81 radiosonde data, and atmospheric modeling (Mesinger et al. 2006). For soil moisture, we used  
82 NLDAS-2 data modeled with the Noah land-surface model (Xia et al. 2012). We also evaluated  
83 three-dimensional reanalysis climate data using the Modern-Era Retrospective Analysis for  
84 Research and Applications (MERRA; Rienecker et al. 2011). Geographic resolution of MERRA  
85 data ranges from  $0.5\text{--}1.25^\circ$  and temporal coverage is 1979–2014. Data are available at a vertical  
86 resolution of 25 hPa from the surface to 700 hPa, and a resolution of 50 hPa for 700–100 hPa.  
87 Climate indices evaluated were the Pacific Decadal Oscillation (PDO; Mantua et al. 1997), the  
88 Southern Oscillation Index (SOI; Trenberth 1984), and the Pacific North American pattern  
89 (PNA; based upon Wallace and Gutzler 1981 but with the modified point-wise method described  
90 at [www.cpc.ncep.noaa.gov/products/precip/CWlink/pna/month\\_pna\\_index2.shtml](http://www.cpc.ncep.noaa.gov/products/precip/CWlink/pna/month_pna_index2.shtml)).

91  
92 We utilized the ensemble of monthly climate model projections made for the fifth phase of the  
93 Coupled Model Intercomparison Project (CMIP5) using the Intergovernmental Panel on Climate

94 Change (IPCC) historical experiment through 2005 and the emissions scenario RCP 8.5 for  
95 2006–2100 (anthropogenic radiative forcing is  $\sim 8.5 \text{ Wm}^{-2}$  by 2100; Moss et al. 2010; van  
96 Vuuren et al. 2011). A list of the 37 models considered is provided in Supplemental Table S1.  
97 For temperature, precipitation, dew point, and wind speed, we created monthly time series for the  
98 SW by linearly interpolating monthly climate fields to  $0.25^\circ$  geographic resolution and  
99 calculating the mean monthly value of grid cells within the SW. We calculated monthly modeled  
100 VPD as in Williams et al. (2013). We also calculated modeled projections of the PDO index, the  
101 SOI, and the PNA index. We calculated the PDO index following Lapp et al. (2011), the PNA  
102 index using the modified point-wise method, and the SOI as the difference in surface pressure  
103 between Tahiti and Darwin (Trenberth 1984). All model realizations of climate have biases in  
104 terms of mean and variance. For each variable, we standardized all model realizations of climate  
105 to a mean of zero and a standard deviation of one (i.e., z-scores) during 1961–2005. We  
106 measured magnitudes of future climate changes as the ensemble-median and inner-quartile  
107 anomalies averaged across 2035–2079 versus those for 1961–2005. Ensemble-median and inner-  
108 quartile differences between the two time periods were calculated by considering each model  
109 only once, regardless of number of model runs available for each model. Multiple model runs for  
110 a given model were averaged together. For each variable and each model run, we generated  
111 10,000 pseudo-random time series that contain the modeled historical 1961–2005 lag-1  
112 autocorrelation and variability to determine 95% and 99% confidence intervals for significant  
113 anomalies accounting for lag-1 autocorrelation. Interannual variability of modeled SW April–  
114 June dew point, temperature, vapor pressure, saturation vapor pressure, and VPD were evaluated  
115 by removing the long-term projected trend from all modeled annual time series. The long-term  
116 projected trend for each variable was developed in 3 steps. First each model run for the historic

117 and future scenario was smoothed with a 31-year filter. Then all 31-year smoothed time series  
118 were averaged together to create a single smoothed record for 1900–2099 for each model. Next,  
119 the long-term projected trend is calculated as the ensemble-median smoothed record, where  
120 decadal variability is cancelled out due to the large number of models and multiple runs  
121 considered for many models. Finally, the long-term trend was removed from each model run by  
122 linearly fitting the long-term trend to each model’s annual 1900–2099 annual time series,  
123 averaged across all runs, and then subtracting the adjusted trend from each annual time series.  
124 Variabilities of the resulting detrended time series were analyzed.

125

### 126 **3. Results and Discussion**

#### 127 **3.1. Drought anomalies in 2011**

128 We expect that temperature, precipitation, VPD, and dew point are all related and that anomalies  
129 in all these variables influenced the anomalous drought conditions in 2011. For each variable, we  
130 identified the window of three or more consecutive months during August 2010 through July  
131 2011 when average SW conditions were most anomalous relative to 1895–2013 (2014 not  
132 included here because July 2014 data were not yet available). Figure 1 indicates that these four  
133 climate variables had strong anomalies in the months before and during the peak drought  
134 conditions and wildfire season of spring and early summer, 2011. These windows were January–  
135 July for precipitation total (Fig. 1a), March–July for  $T_{\max}$  (Fig. 1b), May–July for dew point (Fig.  
136 1c), and March–July for VPD (Fig. 1d). Maps in Figure 1 indicate that sub-regional anomalies  
137 for precipitation, dew point, and VPD exceeded 6 standard deviation units ( $\sigma$ ) in parts of east  
138 New Mexico, west and north Texas, and southwest Oklahoma. Anomalies for dew point were, by  
139 far, the strongest among the variables evaluated. Averaged across the SW, the May–July dew

140 point anomaly was  $-4.6 \sigma$  ( $-3.7 \sigma$  relative to 1961–2013). This dew-point anomaly was expressed  
141 as a vapor-pressure anomaly of  $-3.9 \sigma$ , or  $-21\%$  ( $-3.2 \sigma$ ,  $-20\%$  relative to 1961–2013) and  $10\%$   
142 lower than the second most anomalous May–July vapor-pressure value in 1971.  $T_{\max}$  anomalies  
143 were not as severe when averaged across the SW ( $5^{\text{th}}$  highest on record for March–July), but  
144 anomalies reached  $+4 \sigma$  in east New Mexico and parts of Texas and were highest on record when  
145 averaged across the portion of the SW east of  $105^{\circ}\text{W}$ . March–July  $T_{\min}$  was also high in this  
146 portion of the SW ( $3^{\text{rd}}$  highest on record).

147

148 Although March–July  $T_{\max}$  and  $T_{\min}$  anomalies were only  $+1.9 \sigma$  and  $+1.7 \sigma$ , respectively, when  
149 averaged across the SW ( $+1.7 \sigma$  and  $+1.2 \sigma$  relative to 1961–2013), the March–July VPD  
150 anomaly was  $+3.2 \sigma$  ( $+2.6 \sigma$  relative to 1961–2013). Part of the discrepancy between  
151 temperature and VPD anomalies was due to a disproportionately large influence of strong  $T_{\max}$   
152 anomalies in the eastern SW (caused by the exponential influence of temperature on VPD).  
153 However, the 2011 VPD anomaly was also strongly influenced by extremely low specific  
154 humidity, shown in Fig. 1c. In Figure 2, red and blue lines indicate contributions of temperature  
155 and dew point variability, respectively, toward VPD anomalies (black line) during March–July,  
156 the period when VPD was most anomalous. Dew-point contributions were calculated by holding  
157 monthly temperatures within each PRISM grid cell at their climatological means and only  
158 allowing dew point to vary. Temperature contributions were calculated oppositely. Although  
159 temperature normally dominates VPD variability in the SW (Seager et al. in review),  
160 exceptionally low dew point in 2011 was responsible for  $45\%$  of the VPD anomaly in March–  
161 July 2011 ( $57\%$  when only May–July is considered). The powerful impact of low dew point on  
162 VPD in 2011 is in contrast to the more negligible impact of dew-point anomalies during other

163 recent temperature-driven anomalous VPD years such as 2000–2002, 2006, and 2012 (Fig. 2),  
164 highlighting the uniqueness of the 2011 drought event.

165

### 166 **3.2. Causes of low humidity and high VPD in 2011**

167 Although VPD was anomalously high during all spring and summer months, we focus for the  
168 rest of this paper on April–June (AMJ), the three months centered within the most anomalous  
169 period. In 2011, sustained upper-level convergence occurred above and to the west (upwind) of  
170 the SW (Fig. 3b) as a result of the wave train of circulation anomalies likely associated with the  
171 La Niña sea-surface temperature (SST) pattern and reduced atmospheric heating over the tropical  
172 Pacific Ocean (Fig. 3h). Consistent with La Niña-like atmospheric circulation, upper-level  
173 westerly anomalies above the central and eastern Pacific Ocean were contained within cyclones  
174 straddling the equator. Poleward and east of these cyclones were enhanced upper-level  
175 anticyclonic circulation patterns which, over the North Pacific, translated into a weaker than  
176 normal Aleutian Low (Fig. 3b,d,f). On the eastern flanks of the upper-level subtropical cyclone  
177 and mid-latitude anticyclone (near the west coast of Mexico), southerly wind anomalies  
178 converged with northerly anomalies above western North America (Fig. 3b,d), forcing  
179 subsidence.

180

181 Figure 4b indicates a large region over the eastern North Pacific where upper-level (300 hPa)  
182 convergence anomalies exceeded  $2\sigma$  (relative to 1979–2014) during AMJ 2011 across the  
183 northwest and southwest flanks of the North Pacific high-pressure zone. In addition to the impact  
184 of upper-level convergence, the northerly flow anomaly in the weaker Aleutian Low was, on its  
185 own, associated with descending motion via balances between advection of planetary vorticity

186 and vortex stretching, and between anomalous cold (northerly) advection and compressional  
187 warming. Reanalysis data indicate that AMJ 2011 vertical velocities averaged across the SW  
188 between the surface and 300 hPa were anomalously downward (Fig. 4d), with AMJ 2011  
189 downward velocities ranking second strongest on record according to MERRA and strongest on  
190 record according to the North America Regional Reanalysis (NARR; Mesinger et al. 2006; see  
191 Supplemental section S1). Figure 4d indicates that 2011 vertical-velocity anomalies (MERRA)  
192 were spatially heterogeneous, with subsidence anomalies exceeding  $2-3 \sigma$  throughout much of  
193 Arizona and New Mexico, and ascending anomalies in west Texas. Figure 4e,f shows the vertical  
194 structure of specific humidity and the northwesterly wind pattern traveling along the average  
195 low-level wind path from the coastal northeast Pacific toward and across the SW (path indicated  
196 by the orange line in Fig. 4c). This profile view indicates that the subsidence anomalies  
197 described above were generally present throughout the atmospheric profile upwind of and over  
198 the SW (Fig. 4f).

199  
200 Subsidence brings dry, high altitude air to the surface and contributes to enhanced low-level  
201 divergence. According to NLDAS-2 hourly surface wind data, AMJ 2011 wind speed averaged  
202 across the SW was  $2.6 \sigma$  (18%) above the 1979–2014 mean and surface wind divergence  
203 anomalies were  $>2 \sigma$  across much of the SW (not shown). Divergence of dry, rapidly moving air  
204 over the SW worked to suppress low-level moisture fluxes from the usual sources in the  
205 subtropical Pacific and Gulf of Mexico regions (Fig. 4g,h, southerly surface moisture flux  
206 anomalies into the SW were  $-0.5$  to  $-2 \sigma$ ). This is corroborated by a moisture-tagging experiment  
207 (see Supplemental section S2), indicating that SW atmospheric moisture transported from the  
208 subtropical Pacific and Gulf of Mexico regions was substantially reduced in 2011.

209

210 Low-level humidity in the SW was further suppressed by low evaporation rates from land due to  
211 very dry soils, which resulted from low precipitation in preceding months. Near-surface (0–10  
212 cm) modeled soil moisture averaged across the SW was the lowest on record ( $-2.1 \sigma$ ), causing  
213 evapotranspiration to be the lowest on record ( $-2.0 \sigma$ ) despite record-breaking *potential*  
214 evapotranspiration ( $2.2 \sigma$ ) (anomalies based on 1979–2014 NLDAS-2). Based on our vapor-  
215 tagging analysis, water vapor derived from land-surface evaporation in and around the SW was  
216 virtually missing from the eastern portion of the SW atmosphere in AMJ 2011 (Supplemental  
217 section S2). Continuous exposure to dry westerly winds and high sensible heat flux due to very  
218 dry soils combined to cause record-breaking spring and early summer temperature anomalies  
219 throughout much of west Texas, further amplifying VPD in this region.

220

### 221 **3.3. Interrelation among variables underlying unique 2011 conditions**

222 Figure 5 shows how atmospheric circulation (wind speed and geopotential height) and surface  
223 temperatures correlated with SW dew point (panels on left) and temperature (panels on right)  
224 during AMJ 1979–2013. Importantly, there are strong similarities between the conditions  
225 typically associated with low dew points (Fig. 5, left panels) and the climate anomalies in 2011  
226 (Figure 3). There is less correspondence between anomalies in 2011 and the conditions typically  
227 associated with high temperature (Fig. 5, right panels).

228

229 Correspondence between the 2011 anomaly maps in Figure 3 and the dew-point correlation maps  
230 in Figure 5 indicates that AMJ 2011 climate was in many ways an amplification of the same  
231 atmospheric and oceanic conditions responsible for low dew points in the SW during other years

232 in recent decades. In particular, the 2011 anomaly patterns and dew-point correlation fields share  
233 a sea-level pressure (SLP) gradient between the North Pacific High and low pressure over central  
234 North America (Figs. 3f, 5e). Considering 1961–2014, the AMJ SLP gradient ( $SLP_g$ ) between  
235 the North Pacific (20–45°N, 90–110°W) and North America (30–50°N, 130–170°W) was  
236 strongest on record in 2011 ( $2.8 \sigma$ ) and correlates negatively with AMJ dew point in the SW ( $r =$   
237  $-0.59$ , Table 1; see Supplemental section S3 for methods to calculate  $SLP_g$ ). A strong  $SLP_g$   
238 drives northerly winds down the North American coast, exposing the SW to anomalously dry air  
239 from the north and from above via subsidence. Strong  $SLP_g$  and low SW dew point are  
240 associated with SST patterns resembling the cold phase of the PDO and La Niña (Figs. 3h, 5g),  
241 where intensified  $SLP_g$  promotes, and is reinforced by, northerly low-level wind that drives  
242 upwelling of cold water in the eastern North Pacific. SW dew point may be also partially  
243 suppressed during cold-phase years because relatively cool SSTs suppress atmospheric moisture  
244 across large spatial scales. During 1961–2014, AMJ the PDO correlated positively, and the  
245 Southern Oscillation Index (SOI) correlated negatively, with SW dew point ( $r = 0.47$  and  $-0.46$ ,  
246 respectively; Table 1). Crimmins (2010) shows that La Niña and the PDO cold phase correspond  
247 positively with the frequency of days during which meteorology is conducive to wildfire in the  
248 SW.

249  
250 Another key similarity between the 2011 anomalies and the conditions generally associated with  
251 low SW dew point is a strengthened mid- and upper-level geopotential height gradient between  
252 anomalously low heights over the Pacific Northwest United States and anomalously positive  
253 heights over the eastern North Pacific and western Mexico. These strong gradients promote mid-  
254 and upper-level convergence and subsidence anomalies upwind of and above the SW (Fig. 3b,

255 5a). To represent the strength of these upper-atmospheric pressure gradients and associated  
256 convergence/subsidence processes, we developed a simple geopotential height gradient index  
257 ( $G_{300}$ ) based upon the 300 hPa height patterns in Figs. 3b and 5a. Here,  $G_{300}$  is the mean of two  
258 height gradients (gradient #1: North Pacific minus Pacific Northwest; gradient #2: west Mexico  
259 minus Pacific Northwest; North Pacific: 35–50°N, 160–142°W; Pacific Northwest: 40–50°N,  
260 125–107.5°W; west Mexico: 17.5–30°N, 122.5–97.5°W).  $G_{300}$  is strongly related to  $SLP_g$  ( $r =$   
261 0.87; Table 1) and correlates negatively with SW dew point ( $r = -0.65$ ; Table 1). Positive  $G_{300}$   
262 tends to correspond with the negative phase of the Pacific/North American (PNA) index, which  
263 tends to be favored by cold (La-Niña) phases of the SOI or PDO (Table 1) (Zhang et al. 1997;  
264 Ault et al. 2011), yet may also result from internal variability.

265  
266 Land-surface moisture in 2011 also had a similar spatial anomaly pattern (Fig. 6a) to that  
267 associated with low SW dew point historically (Fig. 6b). Historically, low dew point has  
268 corresponded with dry soil across much of the SW and northern Mexico, and wet soil in the  
269 Pacific Northwest, similar to spatial structures for precipitation and temperature in Figure 1. This  
270 is due partly to the influences that the SOI and PDO oscillations have on the geographic  
271 distribution of winter and spring precipitation in western North America (e.g., Dettinger et al.  
272 1998), which subsequently impact warm-season humidity and temperature (Table 1). Positive  
273 SOI and negative PDO also tend to enhance  $SLP_g$  and  $G_{300}$ , promoting northerly wind and cool  
274 temperatures throughout much of the west (as in Fig. 1d). However, enhanced subsidence,  
275 decreased cloud shading, and increased surface wind speed combine to increase temperature and  
276 potential evapotranspiration toward the eastern SW, drawing soil moisture down and increasing  
277 surface sensible heat fluxes when soil moisture is limiting, as in 2011. The resultant spatial

278 structure of surface temperature and moisture in 2011 may have further promoted high VPD in  
279 the SW via land-surface feedbacks on large-scale atmospheric circulation (e.g., enhancement of a  
280 surface heat low and tropospheric ridging) that reinforced low humidity and high surface  
281 temperature throughout much of the SW, as in the European heat wave of 2003 (e.g., Zaitchik et  
282 al. 2006; Fischer et al. 2007). Therefore, although extreme 2011-like years appear possible only  
283 when a suite of factors are in place, many of these factors are interrelated and may be largely  
284 distilled down to factors that promote dry soils (primarily low precipitation) and strong, dry wind  
285 sourced from the north (primarily  $G_{300}$  and  $SLP_g$ ).

286

### 287 **3.4. Implications for the future**

288 Figure 7 shows CMIP5 ensemble-median (red bars) and inner-quartile climate-model projections  
289 of climate anomalies during 2035–2079 (relative to 1961–2005) for the variables that appear to  
290 have contributed to the extreme 2011 VPD event in the SW. Black bars show 2011 anomalies for  
291 comparison. During AMJ, the mean SW temperature anomaly is projected to be +2.87 °C in  
292 2035–2079 (Fig. 7a). The projected warming trend drives an ensemble-median VPD anomaly of  
293 +3.01 hPa during 2035–2079 (19.5% higher than 1961–2005) (Fig. 7b).

294

295 The other component of VPD, atmospheric moisture content, is also projected to rise (Fig. 7c) in  
296 accordance with general increases in atmospheric and ocean temperatures globally. Increasing  
297 atmospheric moisture content mitigates the effect of warming on VPD, but the exponential  
298 Clausius-Clapeyron relationship between temperature and saturation vapor pressure dictates that  
299 VPD would increase due to warming even if atmospheric moisture content increased enough to  
300 maintain constant relative humidity (RH) (Anderson 1936). In reality, models do not project

301 atmospheric moisture increases to maintain stable RH levels in the SW (Fig. 7d). This is partly  
302 because of limited surface moisture in the SW, but also due to moisture divergence trends in the  
303 mean state of the SW atmospheric circulation (Seager et al. in press). Suppressed increases in  
304 atmospheric moisture content work to amplify the effects of warming on SW VPD.

305

306 It appears that the processes involved in suppressing projected increases in atmospheric moisture  
307 content were at work in suppressing 2011 atmospheric moisture content in multiple respects.

308 Considering the climate variables identified in Sections 3.2 and 3.3 as generally associated with  
309 SW dew-point variability and also anomalous in 2011 ( $SLP_g$ ,  $G_{300}$ , October–June precipitation,  
310 PDO, SOI, PNA, and wind speed), Figure 7e–k indicates that ensemble-median projected trends  
311 share the same sign as 2011 anomalies for all variables evaluated (though projected trends are  
312 very weak for some variables). While the ensemble-median trend in  $SLP_g$  is relatively weak, the  
313 spatial pattern of ensemble-median projected SLP trends is similar to that associated with low  
314 SW dew point (Figs 3,5) and 35 of the 36 models evaluated converge upon increased SLP over  
315 the northeast Pacific Ocean in the region of the Aleutian Low (Supplemental Fig. S4). The  
316 projections evaluated here suggest that some of the large-scale processes projected to suppress  
317 future increases in SW atmospheric moisture content in the SW were at work in 2011.

318

319 Model projections of increasing atmospheric moisture imply that the extremely low atmospheric  
320 moisture levels observed in 2011 and the multi-decade decline that began in the early 1990s  
321 should be becoming increasingly improbable (Fig. 8a). The observed decadal trends shown in  
322 Figure 8a are undoubtedly dominated by internal climate variability, but models within the  
323 CMIP5 archive do not tend to simulate the observed level of multi-decadal internal variability.

324 During 1990–2014, observed AMJ dew point declined by 3.82°C (according to linear trend),  
325 corresponding to a vapor-pressure decline of 20.9%. Histograms in Figure 8b,c show the CMIP5  
326 ensemble distribution of linear changes in (b) dew point and (c) vapor pressure during all  
327 possible 25-year periods of the historical scenario (1850–2005). Only one of the 30 models with  
328 adequate data (CSIRO-Mk3-6-0) simulates a 25-year dew-point decline of more than 3.82°C,  
329 and this occurs at the beginning of the 20<sup>th</sup> century in just one of 10 historical runs. This is also  
330 the only model that simulates a 25-year period when vapor pressure declines by 20.9% or more.  
331 The mismatch between observed and modeled decadal variability in atmospheric moisture  
332 content indicates that either the ongoing decline in SW atmospheric moisture is a truly  
333 exceptional event or that the CMIP5 ensemble largely misrepresents decadal atmospheric  
334 moisture variability in the SW. If models do indeed underrepresent decadal variability in SW  
335 atmospheric moisture, this would imply that repeated occurrences of 2011-like atmospheric  
336 moisture anomalies are more likely than projected by the CMIP5 ensemble.

337

338 Enhanced probability of occurrences of 2011-type atmospheric moisture anomalies are also  
339 suggested by an analysis of projected interannual variability in dew point and vapor pressure  
340 (Fig. 9a,b). Even after removal of long-term projected trends (such as that shown in Fig. 8), the  
341 CMIP5 ensemble projects interannual variability of AMJ dew point to be significantly higher ( $p$   
342  $< 0.01$  based on t-test) during 2035–2079 than in 1961–2005 (Fig. 9a; standard deviation  
343 anomalies in Fig. 9 are based on 1961–2005). Importantly, projected increases in dew-point  
344 variability translate to even larger increases in vapor-pressure variability because of the increase  
345 in mean dew point and the exponential relationship between dew point and vapor pressure.  
346 Comparing the two simulated time periods, the ensemble-median frequency of years when

347 vapor-pressure anomaly (departure from projected trend) is negative enough to positively force  
348 VPD by at least 10% of the 1961–2005 mean (requiring a vapor-pressure anomaly of  $\leq -2.4 \sigma$ ) is  
349 three times higher in 2035–2079 than in 1961–2005 (Fig. 9b).

350  
351 Models also tend to project slight increases in AMJ temperature variability (Fig. 9c). Although  
352 these increases are smaller than those for dew point, the non-linear Clausius-Clapeyron relation  
353 leads to significantly increased variability in saturation vapor pressure due to warming.  
354 Ensemble-median variability in saturation vapor pressure increases by 30%, compared to 20%  
355 for vapor pressure. Comparing the two time periods, the ensemble-median frequency of years  
356 when AMJ saturation vapor pressure anomaly is positive enough to positively force VPD  
357 anomalies by at least 10% (requiring a saturation vapor pressure anomaly of  $\geq 1.3 \sigma$ ) of the 1961–  
358 2005 mean by approximately 84% (Fig. 9d). While this relative change is much less than the  
359 three-fold increase projected for vapor pressure (Fig. 9a), the interannual variability of saturation  
360 vapor pressure is approximately 65% larger than variability of actual vapor pressure, dictating  
361 that temperature variability will continue to be the dominant driver of VPD departures from the  
362 background trend (Fig. 9f). Nonetheless, 2011 serves as an example of the potential for extreme  
363 vapor-pressure anomalies to have impactful effects on VPD. Although models generally do not  
364 simulate dew-point and vapor-pressure anomalies as strong as those observed in 2011,  
365 projections of increased interannual variability for these variables suggests increasing likelihood  
366 of repeated 2011-like events where humidity is substantially reduced relative to the projected  
367 trend, contributing to positive VPD anomalies.

368  
369 Combining the lessons learned from analyses of projected trends and variability, it is clear from

370 Figure 7 that warming and suppressed increases in atmospheric moisture content alone are  
371 projected to contribute to an increased frequency of years when VPD matches or exceeds 2011  
372 levels. Superimposed upon the projected increase in mean VPD, interannual variations of  
373 temperature and dew point (e.g., departures of dew point from the projected trend line in Fig. 8)  
374 will have increasingly amplified effects on VPD due to the exponential relationship between  
375 temperature and saturation vapor pressure. Figure 10 demonstrates how VPD would be  
376 influenced by a 2011-type event in the 2050s, where observed 2011 temperature and dew-point  
377 anomalies are superimposed upon mean 2050s levels. Considering March–August, the period  
378 when VPD correlates strongest with SW burned forest area (Williams et al. in press), a 2011-  
379 type event in the 2050s would cause VPD to be 47% higher than the 1961–2005 average and  
380 16% higher than in 2011.

381

#### 382 **4. Summary and Conclusions**

383 2011 was an interesting year in terms of drought-related climate impacts in the SW because it  
384 was not exceptionally warm throughout the parts of Arizona and New Mexico where record-  
385 breaking forest fires occurred. VPD, on the other hand, *was* record-breaking in these areas  
386 because of exceptionally low atmospheric moisture content. Abatzoglou and Kolden (2013) and  
387 Williams et al. (in press) showed that SW annual burned area is closely tied to spring–summer  
388 potential evapotranspiration, VPD, and moisture deficit. These studies make it clear that record-  
389 breaking wildfire activity in 2011 was very likely promoted by record-low precipitation and  
390 record-high VPD.

391

392 Interestingly, VPD, which is normally dominated by temperature, was amplified in 2011 by

393 extremely low atmospheric moisture content. The meteorological conditions responsible for  
394 extremely low atmospheric moisture in 2011 were driven by an interaction of atmospheric,  
395 oceanic, and land-surface conditions. Among the most important contributing factors appear to  
396 have been record-setting low precipitation totals and a record-setting strong sea-level pressure  
397 gradient between the North Pacific Ocean and North America that drove dry northwesterly wind  
398 and subsidence anomalies toward the SW throughout the troposphere. Subsidence over the SW  
399 was enhanced by upper-level convergence associated with the La Niña-forced atmospheric wave  
400 train. Subsidence aloft led to divergence of dry, lower atmospheric winds across Arizona and  
401 much of New Mexico, blocking advection of moist air from both the subtropical Pacific and the  
402 Gulf of Mexico. Convergence of warm, dry winds in eastern New Mexico and west Texas  
403 interacted with exceptionally dry soils to cause record-breaking heat, further amplifying VPD in  
404 these areas.

405  
406 Model projections suggest that 2011 conditions were representative of projected future climate in  
407 limited ways. CMIP5 climate projections tend to agree upon trends toward an enhanced sea-level  
408 pressure gradient between the North Pacific and North America, an enhanced upper-level  
409 pressure gradient between Mexico and the Pacific Northwest that drives convergence and  
410 subsidence upwind of and above the SW, a more negative PDO, and lower October–June  
411 precipitation totals. As atmospheric moisture content increases with warming globally, projected  
412 trends in the variables listed here combine to slow the projected atmospheric moisture increases  
413 in the SW, as indicated by a significant projected decline in SW relative humidity. These  
414 projections do not necessarily indicate increased frequency of 2011-type circulation extremes,  
415 but they nonetheless positively influence the frequency with which 2011 levels of VPD are

416 achieved in the CMIP5 projections. Further, CMIP5 models generally project the interannual  
417 variability of SW dew point to increase, suggesting that large negative deviations of atmospheric  
418 moisture from the background trend, such as that which occurred in 2011, will become  
419 increasingly probable. Increased interannual variability in dew point amplifies the increase in  
420 interannual VPD variability that is already expected due to the exponential Clausius-Clapeyron  
421 response to warming alone.

422

423 Although the exceptional negative atmospheric moisture anomaly in spring–summer 2011 was  
424 unprecedented in the observed record, CMIP5 projections suggest that 2011-like deviations in  
425 atmospheric moisture content from background levels will become increasingly probable as the  
426 globe warms. Importantly, recurrences of 2011-type events when temperature and atmospheric  
427 moisture deviations combine to substantially amplify VPD will be superimposed upon  
428 increasingly warm background temperatures that, on their own, will drive substantial increases in  
429 SW VPD. By the 2050s, average spring–summer VPD is projected to surpass that of 2011.

430 Strong and non-linear relationships between temperature, VPD, and SW burned area (Williams  
431 et al. in press) suggest that 2011-type precipitation and circulation anomalies, superimposed  
432 upon substantially warmer background conditions, could have far more catastrophic wildfire  
433 consequences than in the record-breaking wildfire year of 2011 if fuel characteristics are not  
434 limiting.

435

#### 436 **Acknowledgments**

437 This work was supported by LANL-LDRD and DoE-BER. RS was supported by NOAA awards  
438 NA10OAR4310137 (Global Decadal Hydroclimate Variability and Change) and NSF award

439 EASM2: Linking Near-term Future Changes in Weather and Hydroclimate in Western North  
440 America to Adaptation for Ecosystem and Water Management. Thanks to CD Allen, C Baisan, C  
441 Daly, D Griffin, R Linn, and SA Rauscher for helpful conversations and insights.

442

## 443 **References**

- 444 Abatzoglou, J. T. and C. A. Kolden. 2013. Relationships between climate and macroscale area  
445 burned in the western United States. *International Journal of Wildland Fire* **22**:1003-  
446 1020.
- 447 Anderson, D. B. 1936. Relative humidity or vapor pressure deficit. *Ecology* **17**:277-282.
- 448 Ault, T. R., A. K. Macalady, G. T. Pederson, J. L. Betancourt, and M. D. Schwartz. 2011.  
449 Northern Hemisphere modes of variability and the timing of spring in western North  
450 America. *Journal of Climate* **24**:4003-4014.
- 451 Crimmins, M. A. 2010. Interannual to decadal changes in extreme fire weather event frequencies  
452 across the southwestern United States. *International Journal of Climatology* **31**:1573-  
453 1583.
- 454 Dettinger, M. D., D. R. Cayan, H. F. Diaz, and D. M. Meko. 1998. North-south precipitation  
455 patterns in western North America on interannual-to-decadal timescales. *Journal of*  
456 *Climate* **11**:3095-3111.
- 457 Fischer, E. M., S. I. Seneviratne, P. L. Vidale, D. Lüthi, and C. Schär. 2007. Soil moisture-  
458 atmosphere interactions during the 2003 European summer heat wave. *Journal of Climate*  
459 **20**:5081-5099.
- 460 Hamlet, A. F. and D. P. Lettenmaier. 2005. Production of Temporally Consistent Gridded  
461 Precipitation and Temperature Fields for the Continental United States. *Journal of*  
462 *Hydrometeorology* **6**:330-336.
- 463 Hoerling, M., A. Kumar, R. Dole, J. W. Nielsen-Gammon, J. Eischeid, J. Perlwitz, X.-W. Quan,  
464 T. Zhang, P. Pegion, and M. Chen. 2013. Anatomy of an Extreme Event. *Journal of*  
465 *Climate* **26**:2811-2832.
- 466 Lapp, S. L., J. M. St Jacques, E. M. Barrow, and D. J. Sauchyn. 2011. GCM projections for the  
467 Pacific Decadal Oscillation under greenhouse forcing for the early 21st century.  
468 *International Journal of Climatology* **32**:1423-1442.
- 469 Littell, J. S., D. McKenzie, D. L. Peterson, and A. L. Westerling. 2009. Climate and wildfire area  
470 burned in Western US ecoprovinces, 1916-2003. *Ecological Applications* **19**:1003-1021.
- 471 Mantua, N. J., S. R. Hare, Y. Zhang, J. M. Wallace, and R. C. Francis. 1997. A Pacific  
472 interdecadal climate oscillation with impacts on salmon production. *Bulletin of the*  
473 *American Meteorological Society* **78**:1069-1079.
- 474 Mesinger, F., G. DiMego, E. Kalnay, K. Mitchell, P. C. Shafran, W. Ebisuzaki, D. Jovic, J.  
475 Woollen, E. Rogers, and E. H. Berbery. 2006. North American regional reanalysis.  
476 *Bulletin of the American Meteorological Society* **87**:343-360.
- 477 Miller, P. 2012. Weather gone Wild. National Geographic.
- 478 Mitchell, K. E., D. Lohmann, P. R. Houser, E. F. Wood, J. C. Schaake, A. Robock, B. A.  
479 Cosgrove, J. Sheffield, Q. Duan, L. LLuo, R. W. Higgins, R. T. Pinker, J. D. Tarpley, D.

480 P. Lettenmaier, C. H. Marshall, J. K. Entin, M. Pan, W. Shi, V. Koren, J. Meng, B. H.  
481 Ramsay, and A. A. Bailey. 2004. The multi-institution North American Land Data  
482 Assimilation System (NLDAS): Utilizing multiple GCIP products and partners in a  
483 continental distributed hydrological modeling system. *Journal of Geophysical Research*  
484 **109**:D07S90.

485 Moss, R. H., J. A. Edmonds, K. A. Hibbard, M. R. Manning, S. K. Rose, D. P. van Vuuren, T. R.  
486 Carter, S. Emori, M. Kainuma, and T. Kram. 2010. The next generation of scenarios for  
487 climate change research and assessment. *Nature* **463**:747-756.

488 Nijhuis, M. 2012. Forest fires: Burn out. *Nature* **489**:352-354.

489 Rienecker, N. M., M. J. Suarez, R. Gelaro, R. Todling, J. Bacmeister, E. Liu, M. G. Bosilovich,  
490 S. D. Schubert, L. Takacs, G.-K. Kim, S. Bloom, L. Chen, D. Collins, A. Conaty, and A.  
491 da Silva. 2011. MERRA - NASA's Modern-Era Retrospective Analysis for Research and  
492 Applications. *Journal of Climate* **24**:3624-3648.

493 Rupp, D. E., P. W. Mote, N. Massey, C. J. Rye, R. Jones, and M. R. Allen. 2012. Did human  
494 influence on climate make the 2011 Texas drought more probable? *Bulletin of the*  
495 *American Meteorological Society* **93**:1052-1054.

496 Seager, R., L. Goddard, J. Nakamura, N. Henerson, and D. E. Lee. 2014. Dynamical causes of  
497 the 2010/11 Texas-northern Mexico drought. *Journal of Hydrometeorology* **15**:39-68.

498 Seager, R., A. Hooks, A. P. Williams, B. I. Cook, J. Nakamura, and N. Henderson. in review.  
499 Climatology, variability and trends in United States vapor pressure deficit, an important  
500 fire-related meteorological quantity. *Journal of Applied Meteorology*.

501 Seager, R., J. D. Neelin, I. Simpson, H. Liu, N. Henderson, T. Shaw, Y. Kushnir, M. Ting, and  
502 B. I. Cook. in press. Dynamical and thermodynamical causes of large-scale changes in  
503 the hydrological cycle over North America in response to global warming. *Journal of*  
504 *Climate*.

505 Swetnam, T. W. and J. L. Betancourt. 1990. Fire-southern oscillation relations in the  
506 southwestern United States. *SCIENCE* **249**:1017-1020.

507 Swetnam, T. W. and J. L. Betancourt. 1998. Mesoscale disturbance and ecological response to  
508 decadal climatic variability in the American Southwest. *Journal of Climate* **11**:3128-  
509 3147.

510 Trenberth, K. E. 1984. Signal versus noise in the Southern Oscillation. *Monthly Weather Review*  
511 **112**:326-332.

512 van Vuuren, D. P., J. Edmonds, M. Kainuma, K. Riahi, A. Thomson, K. Hibbard, G. C. Hurtt, T.  
513 Kram, V. Krey, and J.-F. Lamarque. 2011. The representative concentration pathways: an  
514 overview. *Climatic Change* **109**:5-31.

515 Wallace, J. M. and D. S. Gutzler. 1981. Teleconnections in the geopotential height field during  
516 the Northern Hemisphere winter. *Mon. Wea. Rev* **109**:784-812.

517 Westerling, A. L., A. Gershunov, T. J. Brown, D. R. Cayan, and M. D. Dettinger. 2003. Climate  
518 and wildfire in the western United States. *Bulletin of the American Meteorological*  
519 *Society* **84**:595-604.

520 Westerling, A. L., H. G. Hidalgo, D. R. Cayan, and T. W. Swetnam. 2006. Warming and earlier  
521 spring increase western US forest wildfire activity. *SCIENCE* **313**:940-943.

522 Westerling, A. L. and T. W. Swetnam. 2003. Interannual to decadal drought and wildfire in the  
523 western United States. *Eos* **84**:545-554.

524 Williams, A. P., C. D. Allen, A. K. Macalady, D. Griffin, C. A. Woodhouse, D. M. Meko, T. W.  
525 Swetnam, S. A. Rauscher, R. Seager, H. D. Grissino Mayer, J. S. Dean, E. R. Cook, C.

526 Gangodagamage, M. Cai, and N. G. McDowell. 2013. Temperature as a potent driver of  
527 regional forest drought stress and tree mortality. *Nature Climate Change* **3**:292-297.

528 Williams, A. P., R. Seager, M. Berkelhammer, A. K. Macalady, M. A. Crimmins, T. W.  
529 Swetnam, A. T. Trugman, N. Buenning, N. Hryniw, N. G. McDowell, D. Noone, C. I.  
530 Mora, and T. Rahn. in press. Correlations between components of the water balance and  
531 burned area reveal new insights for predicting fire activity in the southwest US.  
532 *International Journal of Wildland Fire*.

533 Xia, Y., K. Mitchell, M. B. Ek, J. Sheffield, B. A. Cosgrove, E. Wood, L. Luo, C. Alonge, H.  
534 Wei, J. Meng, B. Linvneh, D. P. Lettenmaier, V. Koren, Q. Duan, K. Mo, Y. Fan, and D.  
535 Mocko. 2012. Continental-scale water and energy flux analysis and validation for the  
536 North American Land Data Assimilation System project phase 2 (NLDAS-2): 1.  
537 Intercomparison and application of model products. *Journal of Geophysical Research*  
538 **117**:D03109.

539 Zaitchik, B. F., A. K. Macalady, L. R. Beonneau, and R. B. Smith. 2006. Europe's 2003 heat  
540 wave: a satellite view of impacts and land-atmosphere feedbacks. *International Journal*  
541 *of Climatology* **26**:743-769.

542 Zhang, Y., J. M. Wallace, and D. S. Battisti. 1997. ENSO-like interdecadal variability: 1900-93.  
543 *Journal of Climate* **10**:1004-1020.

544

545

546

547

548

549

550

551

552

553

554

555

556

557

558

559

560 **Table 1.** Correlation matrix for 11 interrelated climate variables that influenced extreme SW drought in  
561 2011. All climate records represent April–June except precipitation (October–June). Correlations  
562 represent 1961–2014 except for those involving  $G_{300}$  or soil moisture ( $soil_m$ ) (1979–2014). Bold values:  
563 correlations significant above 95% confidence, accounting for lag-1 autocorrelation. NLDAS-2 wind-  
564 speed data were extended to 1961 using Sheffield et al. (2006) dataset.

565

|                         | <b>VPD</b>  | <b>T<sub>ave</sub></b> | <b>T<sub>dew</sub></b> | <b>SLP<sub>g</sub></b> | <b>G<sub>300</sub></b> | <b>Soil<sub>m</sub></b> | <b>Precip</b> | <b>Wind</b>  | <b>PDO</b>   | <b>SOI</b>   | <b>PNA</b>   |
|-------------------------|-------------|------------------------|------------------------|------------------------|------------------------|-------------------------|---------------|--------------|--------------|--------------|--------------|
| <b>VPD</b>              | <b>1.00</b> | <b>0.85</b>            | <b>-0.58</b>           | <b>0.30</b>            | 0.27                   | <b>-0.89</b>            | <b>-0.75</b>  | <b>0.40</b>  | -0.19        | <b>0.32</b>  | <b>-0.28</b> |
| <b>T<sub>ave</sub></b>  | -           | <b>1.00</b>            | -0.09                  | 0.00                   | -0.09                  | <b>-0.66</b>            | <b>-0.51</b>  | 0.07         | 0.01         | 0.09         | -0.15        |
| <b>T<sub>dew</sub></b>  | -           | -                      | <b>1.00</b>            | <b>-0.59</b>           | <b>-0.65</b>           | <b>0.79</b>             | <b>0.68</b>   | <b>-0.65</b> | <b>0.47</b>  | <b>-0.46</b> | <b>0.37</b>  |
| <b>SLP<sub>g</sub></b>  | -           | -                      | -                      | <b>1.00</b>            | <b>0.87</b>            | <b>-0.49</b>            | -0.22         | <b>0.60</b>  | <b>-0.32</b> | <b>0.39</b>  | <b>-0.59</b> |
| <b>G<sub>300</sub></b>  | -           | -                      | -                      | -                      | <b>1.00</b>            | <b>-0.51</b>            | <b>-0.34</b>  | <b>0.84</b>  | <b>-0.39</b> | 0.33         | <b>-0.56</b> |
| <b>Soil<sub>m</sub></b> | -           | -                      | -                      | -                      | -                      | <b>1.00</b>             | <b>0.90</b>   | <b>-0.72</b> | <b>0.39</b>  | <b>-0.46</b> | <b>0.50</b>  |
| <b>Precip</b>           | -           | -                      | -                      | -                      | -                      | -                       | <b>1.00</b>   | <b>-0.50</b> | <b>0.36</b>  | <b>-0.40</b> | <b>0.34</b>  |
| <b>Wind</b>             | -           | -                      | -                      | -                      | -                      | -                       | -             | <b>1.00</b>  | <b>-0.35</b> | <b>0.49</b>  | <b>-0.49</b> |
| <b>PDO</b>              | -           | -                      | -                      | -                      | -                      | -                       | -             | -            | <b>1.00</b>  | <b>-0.34</b> | <b>0.57</b>  |
| <b>SOI</b>              | -           | -                      | -                      | -                      | -                      | -                       | -             | -            | -            | <b>1.00</b>  | <b>-0.39</b> |
| <b>PNA</b>              | -           | -                      | -                      | -                      | -                      | -                       | -             | -            | -            | -            | <b>1.00</b>  |

566

567

568

569

570

571

572

573

574

575

576

577 **Figure Captions**

578 **Figure 1.** Surface climate anomalies in 2011 for log(precipitation) (a), daily maximum  
579 temperature (b), dew point (c), and VPD (d). For each variable, this figure shows the period of  
580 3–6 months during August 2010 through July 2011 with the strongest anomaly in the SW. Maps  
581 show spatial distributions of anomalies as standard deviations from the 1895–2013 mean. Time  
582 series show annual values averaged across the SW region, with red dots indicating 2011 values.  
583 In maps, red polygons bound the SW, black contours represent drought anomalies of 2 standard  
584 deviations, and yellow areas indicate locations of 2011 fires (Williams et al. in press).

585  
586 **Figure 2.** March–July VPD anomalies (departure from the 1961–2013 mean of 15.17 hPa). Red  
587 and blue lines indicate partial contributions of temperature and dew point anomalies,  
588 respectively, toward the total anomaly (thick black). Partial contributions of temperature and dew  
589 point anomalies were calculated by only allowing one variable at a time to vary from its 1961–  
590 2013 mean.

591  
592 **Figure 3.** April–June atmospheric circulation and surface temperature. Left panels: 1979–2014  
593 means. Right panels: 2011 standardized anomalies. Arrow vectors: vertically integrated wind  
594 velocity. Panels (a and b): upper troposphere (300–200 hPa), background is 300 hPa geopotential  
595 height. Panels (c and d): middle troposphere (600–400 hPa), background is 500 hPa geopotential  
596 height. Panels (e and f): lower troposphere (surface to 700 hPa), background is sea-level  
597 pressure. Panels (g and h): surface temperature.

598

599 **Figure 4.** April–June three-dimensional atmospheric circulation. Left panels: 1979–2014 means.  
600 Right panels: 2011 standardized anomalies. Panels (a and b): Convergence of wind at 300 hPa  
601 (negative values indicate divergence). Panels (c and d): vertical velocity between surface and 300  
602 hPa (positive values indicate sinking motion). Panels (e and f): vertical atmospheric profiles of  
603 horizontal and vertical winds (arrow vectors) and specific humidity (background) along the  
604 orange path shown in panel (c) from west to east. The path represents the mean trajectory of  
605 wind passing through central SW between the surface and 650 hPa during April–June. The  
606 orange line represents the surface and the maroon area bounded by red lines represents the SW  
607 region. Panels (g and h): integrated atmospheric vapor flux (arrow vectors) and content  
608 (background) between the surface and 650 hPa.

609  
610 **Figure 5.** April–June atmospheric circulation and surface temperature versus SW dew point (left  
611 panels) and temperature (right panels). Analysis period is 1979–2014, excluding 2011 to avoid  
612 biasing correlation fields toward extreme 2011 conditions. Wind-vector directions and color  
613 schemes reflect conditions associated with high VPD (low dew point on left, high temperature on  
614 right) in the SW. Arrow vectors in (a–f): correlation with vertically integrated wind velocity.  
615 Panels (a and b): upper troposphere (300–200 hPa), background is correlation with 300 hPa  
616 geopotential height. Panels (c and d): middle troposphere (600–400 hPa), background is  
617 correlation with 500 hPa geopotential height. Panels (e and f): lower troposphere (surface to 700  
618 hPa), background is correlation with sea-level pressure. Only correlations with > 90% confidence  
619 (accounting for lag-1 autocorrelation) are shown.

620

621 **Figure 6.** April–June 0–10 cm soil moisture anomaly during 2011 (a), and correlation with SW  
622 dew point (b) and temperature (c). Analysis period is 1979–2014, excluding 2011 to avoid  
623 biasing correlation fields toward extreme 2011 conditions. Color scheme in all panels is  
624 organized such that brown colors correspond with low soil moisture in the SW. In (b and c), only  
625 correlations with > 90% confidence (accounting for lag-1 autocorrelation) are shown.

626

627 **Figure 7.** CMIP5 climate projections. Red bars: ensemble-median of the average annual  
628 anomaly during 2035–2079 relative to 1961–2005. Whiskers: ensemble inner-quartile anomalies.  
629 Black bars: 2011 anomalies. Projected mean anomalies in 2035–2079 that fall within the dark  
630 and light grey areas are not significant at the 95% and 99% confidence levels, respectively,  
631 accounting for lag-1 autocorrelation in model data. Units of anomalies are standard deviations  
632 from the 1961–2005 mean, based on variability during that period. Red values on the left  
633 indicate absolute values of the ensemble-median anomalies based upon 1961–2005 observed  
634 variability. All variables represent April–June except for precipitation, which represents  
635 October–June. N indicates the number of models with required data.

636

637 **Figure 8.** Observed AMJ dew point in the SW during 1961–2014 overlaid on the CMIP5  
638 ensemble-median (thick black curve) and inner-quartile trends (grey shading) trends. Dotted  
639 curves indicate standard deviation departures from the ensemble-median trend, based on 1961–  
640 2005 observed variability. Model time series were adjusted to exhibit observed variability during  
641 1961–2005 (the period when the observed record overlaps with the historical model simulations)  
642 and the observed mean during 1961–2014.

643

644 **Figure 9.** Modeled interannual variability for historic and projected scenarios. Scatter plots  
645 compare interannual variability during 2035–2079 to that of 1961–2005 for AMJ (a) dew point,  
646 (c) temperature, and (e) dew-point depression (temperature minus dew point). Each number  
647 corresponds to a CMIP5 model, listed in Supplemental Table S1. Variability is calculated after  
648 the long-term trend is removed. The magnitude of a standard deviation is based on the 1961–  
649 2005 period. Bar plots compare the frequency of extreme years when interannual anomalies in  
650 AMJ vapor pressure (b), saturation vapor pressure (d), and VPD (f) are strong enough to  
651 positively force VPD by at least 10% of the 1961–2005 mean. Double asterisks (\*\*) above bar  
652 plots indicate significant ( $p < 0.01$ ) differences in simulated frequencies of extreme years for the  
653 two time periods. Arrows in (b and c) indicate observed changes in dew point and vapor pressure  
654 during 1990–2014 (-3.82 hPa and -20.9%, respectively).

655

656 **Figure 10.** Annual VPD cycle. Annual cycles for 1961–2005 and 2011 represent observed data.  
657 Grey shading bounds inner-quartiles of 1961–2005 annual values. Annual cycles for 2050s  
658 represent CMIP5 ensemble means (*lines and circles*) and inner-quartiles (*shading*). For the case  
659 of the 2011-type event in the 2050s, 2011 temperature and dew-point anomalies were  
660 superimposed upon 2050s modeled temperature and dew-point.

661

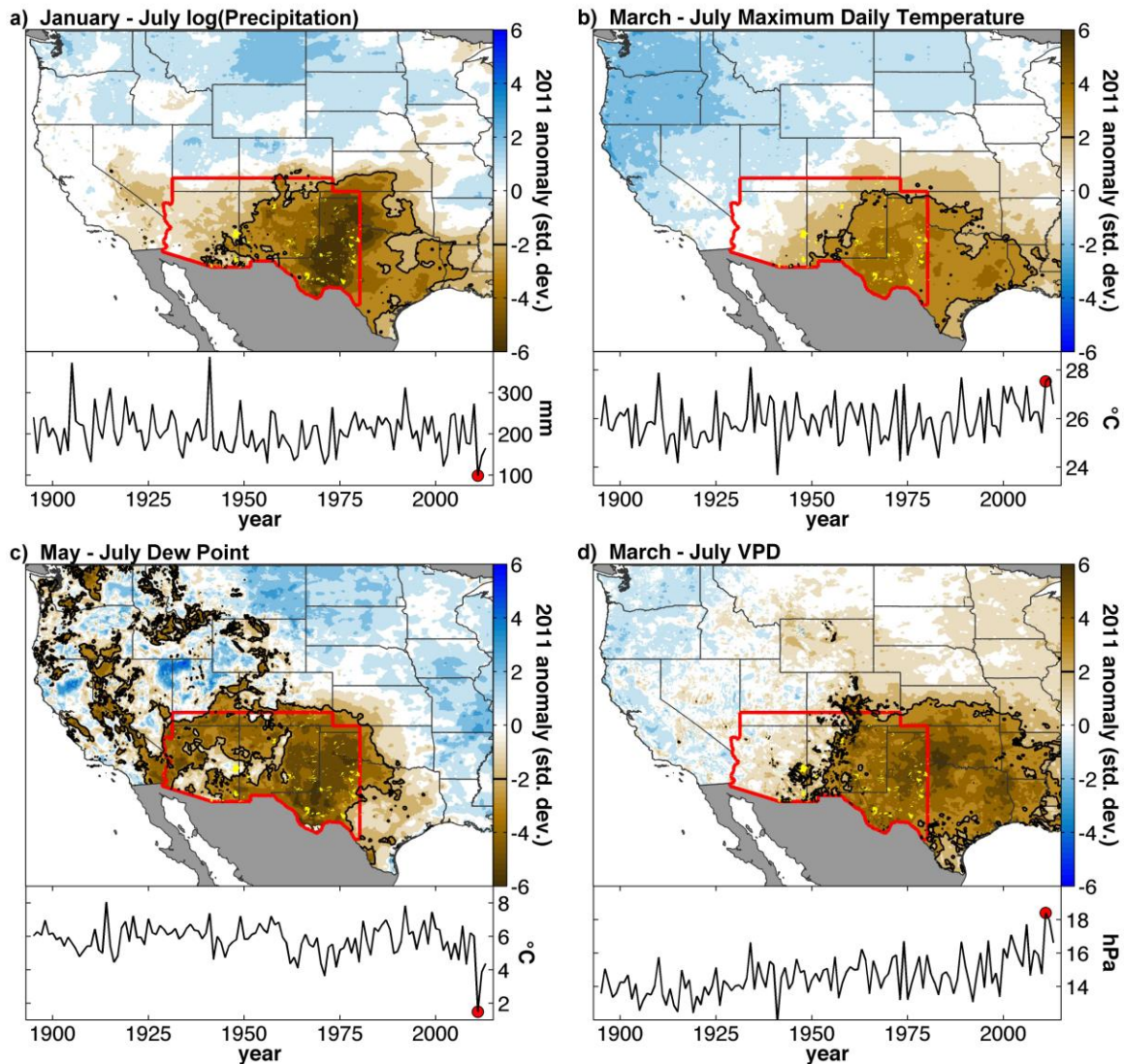
662

663

664

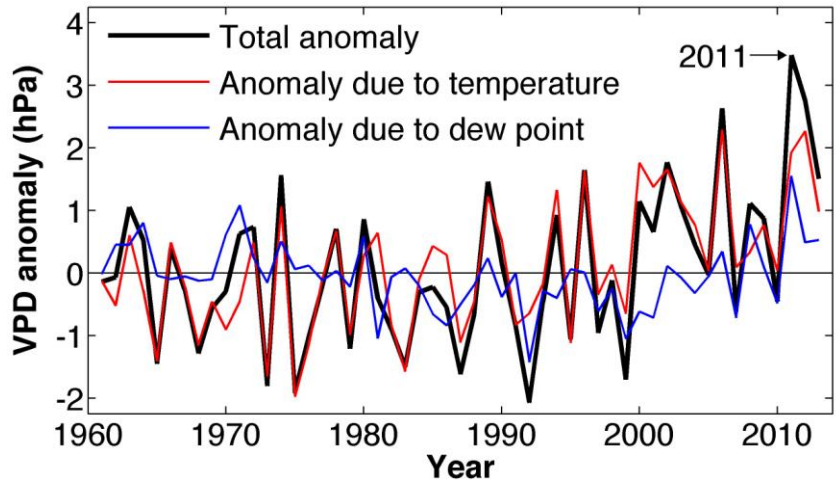
665

666



668 **Figure 1.** Surface climate anomalies in 2011 for log(precipitation) (a), daily maximum temperature (b),  
 669 dew point (c), and VPD (d). For each variable, this figure shows the period of 3–6 months during August  
 670 2010 through July 2011 with the strongest anomaly in the SW. Maps show spatial distributions of  
 671 anomalies as standard deviations from the 1895–2013 mean. Time series show annual values averaged  
 672 across the SW region, with red dots indicating 2011 values. In maps, red polygons bound the SW, black  
 673 contours represent drought anomalies of 2 standard deviations, and yellow areas indicate locations of  
 674 2011 fires (Williams et al. in press).  
 675

676  
 677  
 678  
 679  
 680  
 681  
 682  
 683  
 684



685  
 686 **Figure 2.** March–July VPD anomalies (departure from the 1961–2013 mean of 15.17 hPa). Red and blue  
 687 lines indicate partial contributions of temperature and dew point anomalies, respectively, toward the total  
 688 anomaly (thick black). Partial contributions of temperature and dew point anomalies were calculated by  
 689 only allowing one variable at a time to vary from its 1961–2013 mean.

690  
 691  
 692  
 693  
 694  
 695  
 696  
 697  
 698  
 699  
 700  
 701  
 702  
 703  
 704  
 705  
 706  
 707  
 708  
 709  
 710  
 711  
 712  
 713  
 714  
 715  
 716  
 717  
 718  
 719  
 720  
 721

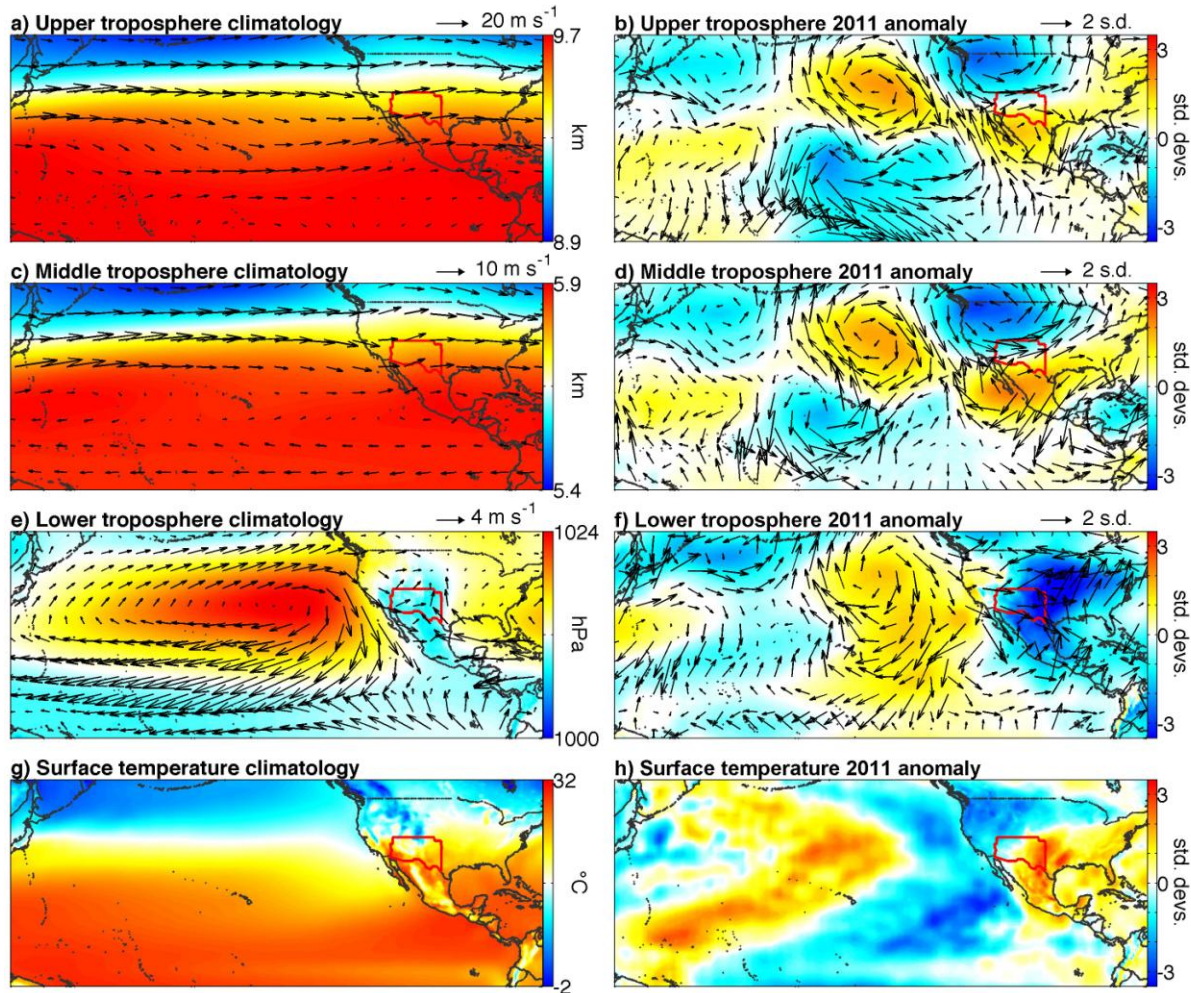
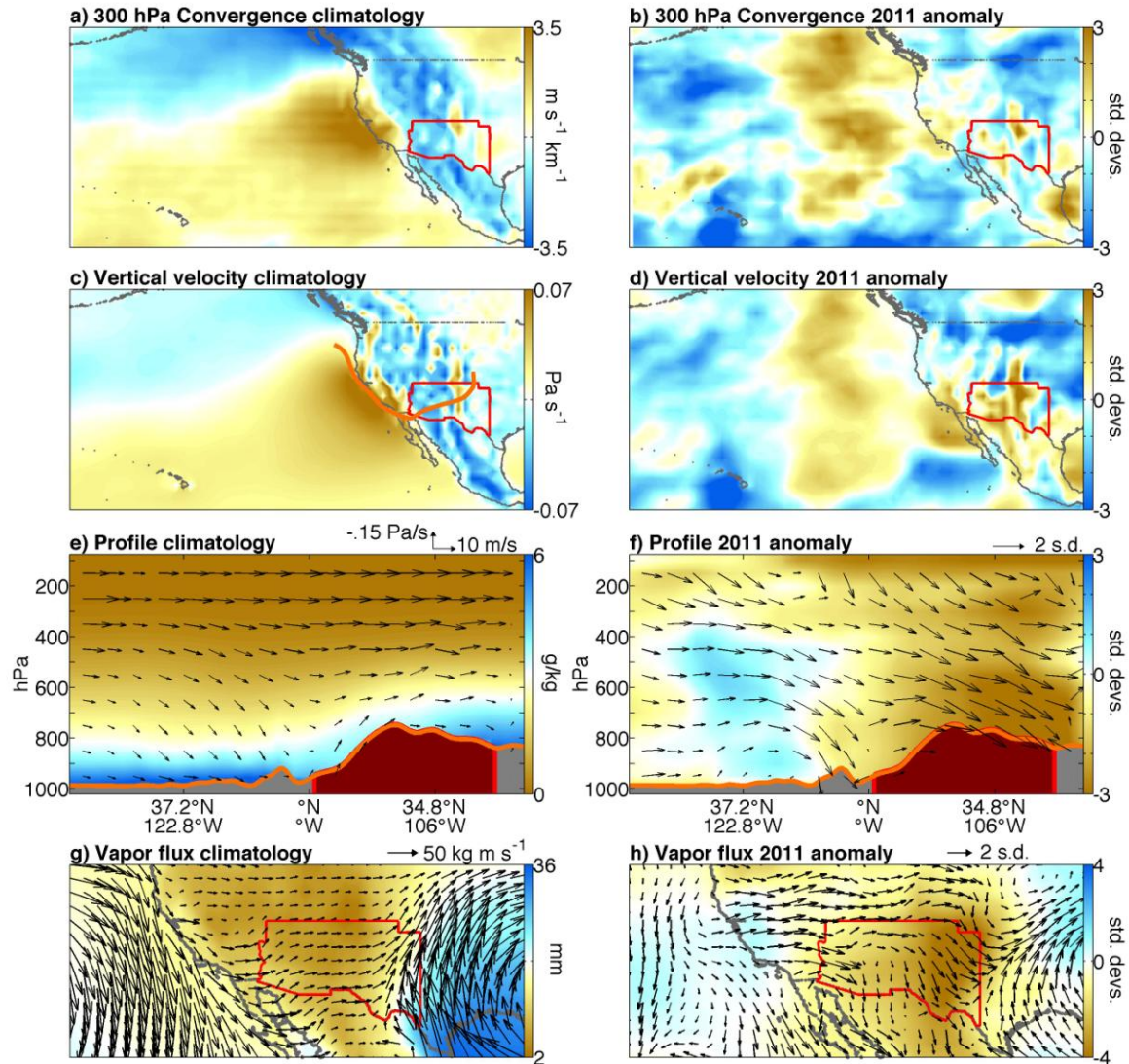


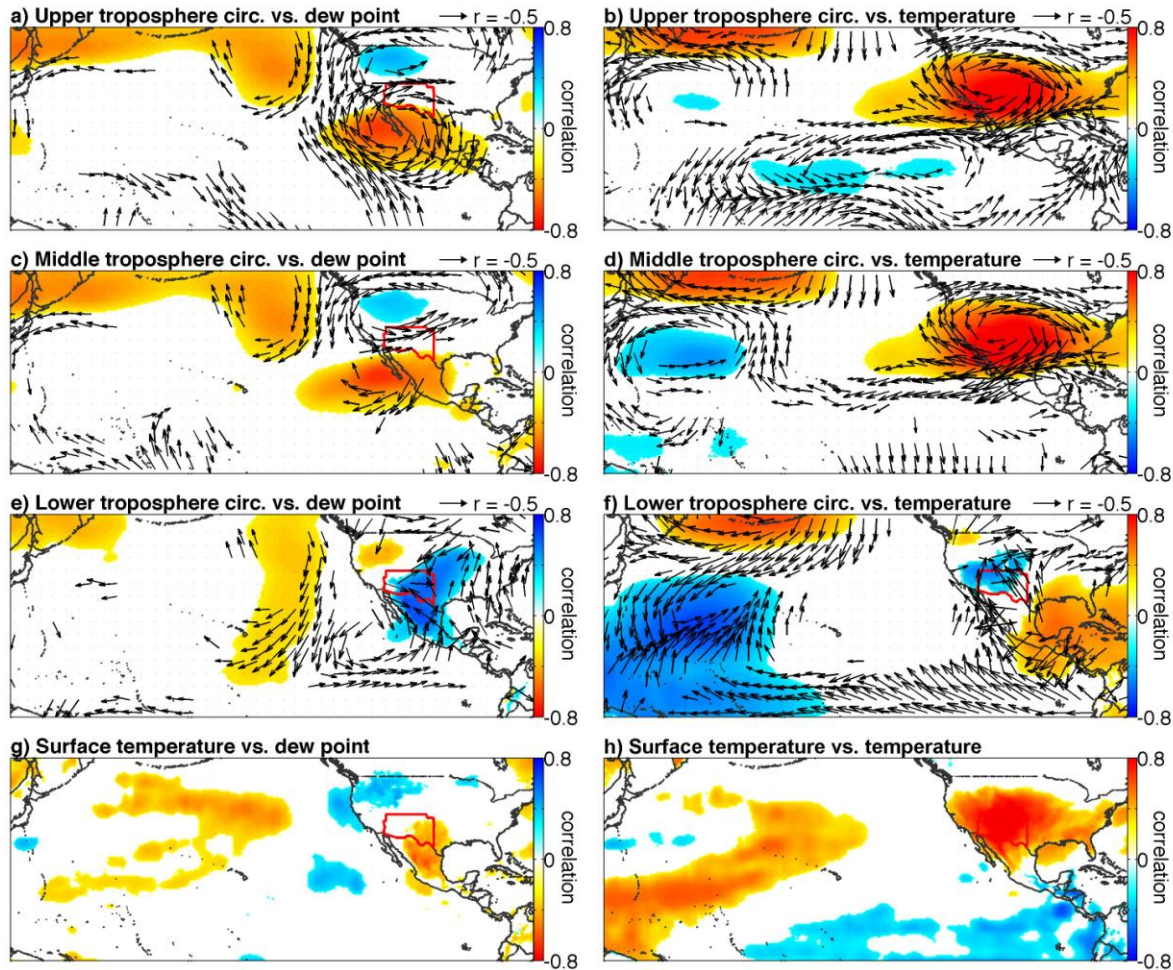
**Figure 3.** April–June atmospheric circulation and surface temperature. Left panels: 1979–2014 means. Right panels: 2011 standardized anomalies. Arrow vectors: vertically integrated wind velocity. Panels (a and b): upper troposphere (300–200 hPa), background is 300 hPa geopotential height. Panels (c and d): middle troposphere (600–400 hPa), background is 500 hPa geopotential height. Panels (e and f): lower troposphere (surface to 700 hPa), background is sea-level pressure. Panels (g and h): surface temperature.

722  
 723  
 724  
 725  
 726  
 727  
 728  
 729  
 730  
 731  
 732  
 733  
 734  
 735  
 736  
 737  
 738  
 739  
 740  
 741  
 742



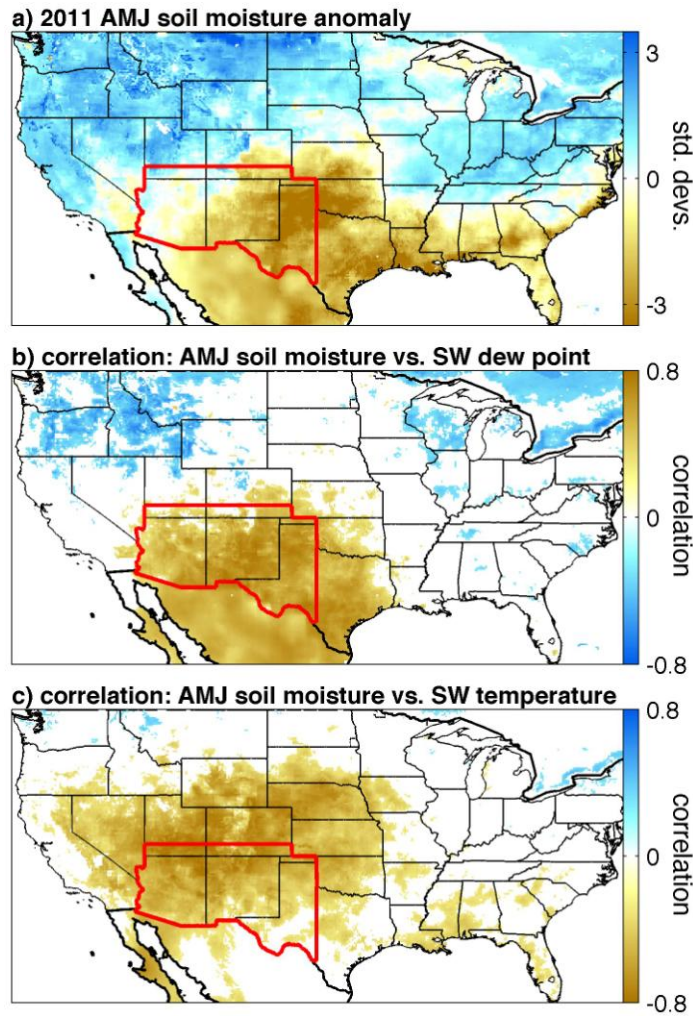
743  
 744 **Figure 4.** April–June three-dimensional atmospheric circulation. Left panels: 1979–2014 means. Right  
 745 panels: 2011 standardized anomalies. Panels (a and b): Convergence of wind at 300 hPa (negative values  
 746 indicate divergence). Panels (c and d): vertical velocity between surface and 300 hPa (positive values  
 747 indicate sinking motion). Panels (e and f): vertical atmospheric profiles of horizontal and vertical winds  
 748 (arrow vectors) and specific humidity (background) along the orange path shown in panel (c) from west to east.  
 749 The path represents the mean trajectory of wind passing through central SW between the surface and  
 750 650 hPa during April–June. The orange line represents the surface and the maroon area bounded by red  
 751 lines represents the SW region. Panels (g and h): integrated atmospheric vapor flux (arrow vectors) and  
 752 content (background) between the surface and 650 hPa.

753  
 754  
 755  
 756  
 757  
 758  
 759  
 760  
 761



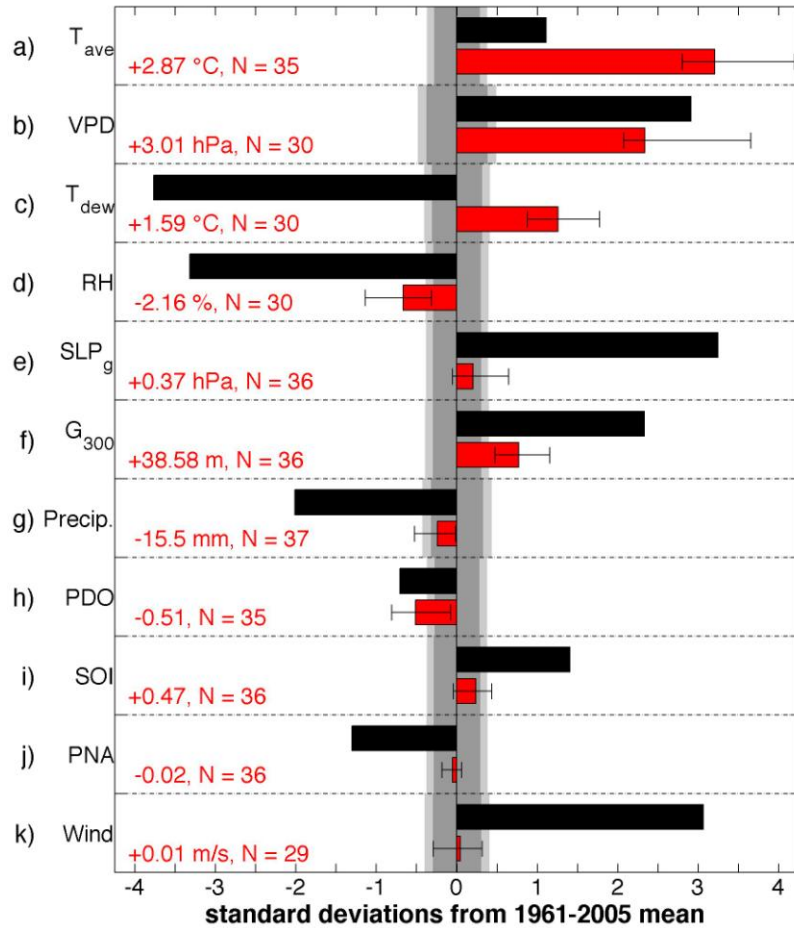
762  
763  
764  
765  
766  
767  
768  
769  
770  
771  
772  
773  
774  
775  
776  
777  
778  
779  
780  
781  
782  
783  
784

**Figure 5.** April–June atmospheric circulation and surface temperature versus SW dew point (left panels) and temperature (right panels). Analysis period is 1979–2014, excluding 2011 to avoid biasing correlation fields toward extreme 2011 conditions. Wind-vector directions and color schemes reflect conditions associated with high VPD (low dew point on left, high temperature on right) in the SW. Arrow vectors in (a–f): correlation with vertically integrated wind velocity. Panels (a and b): upper troposphere (300–200 hPa), background is correlation with 300 hPa geopotential height. Panels (c and d): middle troposphere (600–400 hPa), background is correlation with 500 hPa geopotential height. Panels (e and f): lower troposphere (surface to 700 hPa), background is correlation with sea-level pressure. Only correlations with > 90% confidence (accounting for lag-1 autocorrelation) are shown.



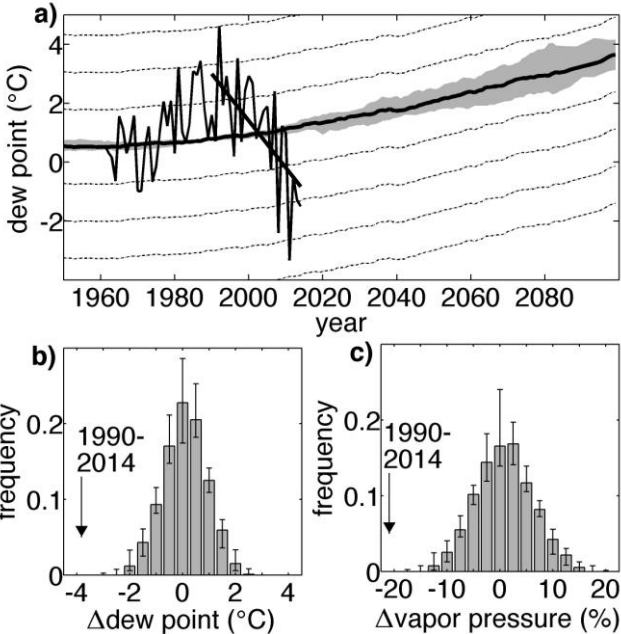
785  
 786 **Figure 6.** April–June 0–10 cm soil moisture anomaly during 2011 (a), and correlation with SW dew point  
 787 (b) and temperature (c). Analysis period is 1979–2014, excluding 2011 to avoid biasing correlation fields  
 788 toward extreme 2011 conditions. Color scheme in all panels is organized such that brown colors  
 789 correspond with low soil moisture in the SW. In (b and c), only correlations with > 90% confidence  
 790 (accounting for lag-1 autocorrelation) are shown.

791  
 792  
 793  
 794  
 795  
 796  
 797  
 798  
 799  
 800  
 801  
 802  
 803  
 804  
 805  
 806



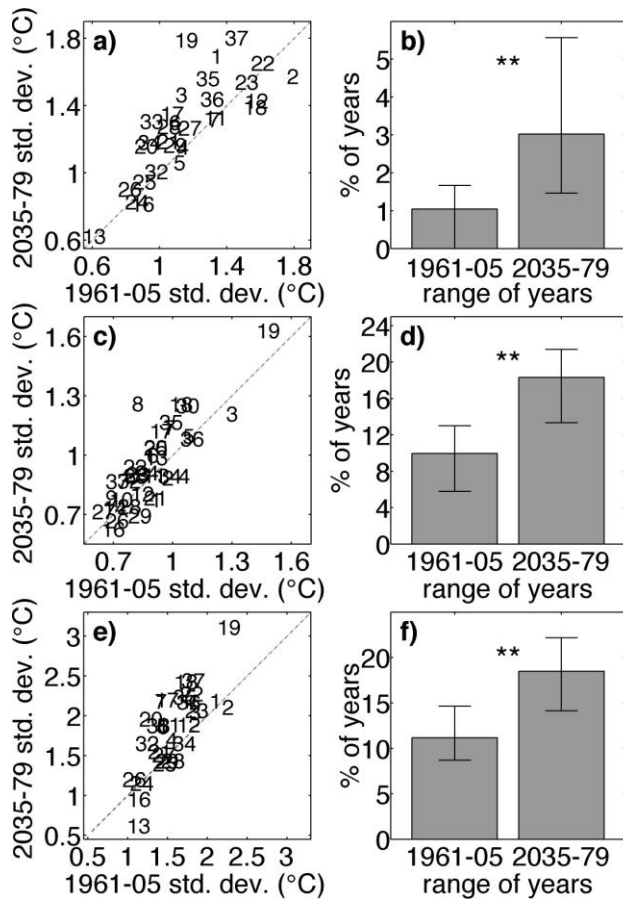
807  
 808 **Figure 7.** CMIP5 climate projections. Red bars: ensemble-median of the average annual anomaly during  
 809 2035–2079 relative to 1961–2005. Whiskers: ensemble inner-quartile anomalies. Black bars: 2011  
 810 anomalies. Projected mean anomalies in 2035–2079 that fall within the dark and light grey areas are not  
 811 significant at the 95% and 99% confidence levels, respectively, accounting for lag-1 autocorrelation in  
 812 model data. Units of anomalies are standard deviations from the 1961–2005 mean, based on variability  
 813 during that period. Red values on the left indicate absolute values of the ensemble-median anomalies  
 814 based upon 1961–2005 observed variability. All variables represent April–June except for precipitation,  
 815 which represents October–June. N indicates the number of models with required data.

816  
 817  
 818  
 819  
 820  
 821  
 822  
 823  
 824  
 825  
 826  
 827  
 828  
 829

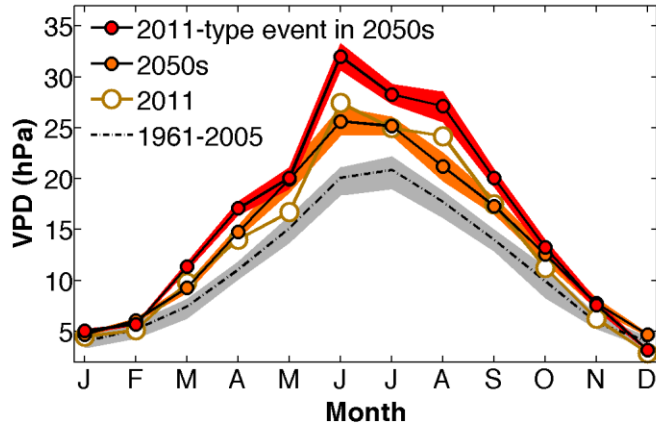


830  
831  
832  
833  
834  
835  
836  
837  
838  
839  
840  
841  
842  
843  
844  
845  
846  
847  
848  
849  
850  
851  
852  
853  
854  
855  
856  
857  
858  
859  
860

**Figure 8.** Observed (1961–2014) and modeled multi-decade variability of AMJ dew point and vapor pressure. (a) Observed record overlaid on CMIP5 ensemble-median (thick black curve) and inner-quartile (grey shading) trends. Dotted curves indicate standard deviation departures from the ensemble-median trend, based on 1961–2005 observed variability. The straight black line shows the linear dew-point trend during 1990–2014, representing 25-year reductions of 3.82°C and 20.9% for dew point and vapor pressure, respectively. Histograms in (b and c) show the CMIP5 ensemble distribution of linear changes in (b) dew point and (c) vapor pressure during all possible 25-year periods of the historical scenario (1850–2005). Bars represent the ensemble-median histogram and whiskers represent inner-quartiles. Arrows in (b and c) indicate observed changes in dew point and vapor pressure during 1990–2014 (-3.82 hPa and -20.9%, respectively).



861  
 862 **Figure 9.** Modeled interannual variability for historic and projected scenarios. Scatter plots compare  
 863 interannual variability during 2035–2079 to that of 1961–2005 for AMJ (a) dew point, (c) temperature,  
 864 and (e) dew-point depression (temperature minus dew point). Each number corresponds to a CMIP5  
 865 model, listed in Supplemental Table S1. Variability is calculated after the long-term trend is removed.  
 866 The magnitude of a standard deviation is based on the 1961–2005 period. Bar plots compare the  
 867 frequency of extreme years when interannual anomalies in AMJ vapor pressure (b), saturation vapor  
 868 pressure (d), and VPD (f) are strong enough to positively force VPD by at least 10% of the 1961–2005  
 869 mean. Double asterisks (\*\*) above bar plots indicate significant ( $p < 0.01$ ) differences in simulated  
 870 frequencies of extreme years for the two time periods.  
 871  
 872  
 873  
 874  
 875  
 876  
 877  
 878  
 879  
 880  
 881  
 882  
 883  
 884



885  
886  
887  
888  
889  
890  
891

**Figure 10.** Annual VPD cycle. Annual cycles for 1961–2005 and 2011 represent observed data. Grey shading bounds inner-quartiles of 1961-2005 annual values. Annual cycles for 2050s represent CMIP5 ensemble means (*lines and circles*) and inner-quartiles (*shading*). For the case of the 2011-type event in the 2050s, 2011 temperature and dew-point anomalies were superimposed upon 2050s modeled temperature and dew-point.

892